Radiation magnetohydrodynamics modeling of an impulsively driven chromospheric jet in the solar atmosphere

J. J. González-Avilés

*Escuela Nacional de Estudios Superiores (ENES), Unidad Morelia, Universidad Nacional Autónoma de México,
Unidad Morelia 58910, Morelia, Michoacán, México.*

In this paper, we present a numerical simulation of an impulsively driven chromospheric jet in the solar atmosphere using the non-ideal magnetohydrodynamic (MHD) equations coupled with frequency- and angle-averaged radiation transport equations. These include the dynamics of the radiation energy density and radiation flux. The jet is initiated by a localized Gaussian pulse applied to the vertical velocity component in the upper chromosphere ($y = 1.75$ Mm), producing a collimated plasma structure that exhibits characteristics similar to macrospicules. We focus on the formation and evolution of the chromospheric jet as it propagates through an optically thin region encompassing the upper chromosphere and solar corona, where both the Planck-averaged absorption and Rosseland-averaged scattering opacities are low. Although radiation transport terms only slightly affect the jet's morphology, they play a significant role in governing radiative processes in the corona. In particular, radiation transport contributes to the dissipation of the chromospheric jet, which effectively acts as a radiative cooling mechanism as the jet evolves through the optically thin solar corona.

1. Introduction

Jets are dynamic plasma ejections in the solar atmosphere, widely observed in both quiet and active regions across multiple wavelengths, including X-rays, Extreme Ultraviolet (EUV), and Hα. To explain these observations, several physical mechanisms have been proposed, both theoretically and numerically, with magnetic reconnection being one of the most widely accepted jet triggering processes [1-3]. Among the various types of jets, spicules are particularly notable. They are thin spike-shaped plasma structures that are predominantly observed in the chromosphere [4]. Depending on their size and lifetime, spicules are commonly classified into three types: (i) Type I spicules, with lengths of 7-11 Mm, lifetimes of 5-15 minutes, and upward velocities around 25 km s^{-1} [5,6]; (ii) Type II spicules, with average heights of 5 Mm, propagation speeds of 50-100 km s^{-1}, and short lifetimes ranging from 10 to 150 seconds [7,8]; (iii) Macrospicules, typically observed in polar coronal holes, reach heights between 7 and 70 Mm above the solar limb, with maximum velocities from 10 to 150 km s^{-1} and lifetimes ranging from 3 to 45 minutes [9,10].

In the context of numerical MHD simulations, a chromospheric jet that exhibits spicule-like features, such as height, vertical velocity, and lifetime, can be modeled as an impulsively driven jet. This type of jet is a dynamic plasma outflow initiated by a spatially localized perturbation (*e.g.*, a pressure pulse, reconnection burst, or velocity pulse) in a magnetized plasma. The resulting disturbance generates a high-speed, narrow jet of material that propagates along magnetic field lines in the solar atmosphere. Several MHD simulations of impulsively driven chromospheric jets reproduce spicule-like

characteristics, including 2D adiabatic, non-adiabatic, and two-fluid models [see, *e.g.*,][11-17]. In all these studies, the jet formation mechanism is based on the classical rebound shock model [18,19], which explains spicule formation as the result of shock waves generated by localized impulsive disturbances. These shocks propel chromospheric plasma upward along magnetic field lines, producing short-lived, narrow jets that closely resemble Type I spicules in both morphology and dynamics. In contrast, the formation of Type II spicules is not attributed to impulsive driving. Instead, 2D and 3D MHD simulations indicate that their generation involves more complex physical processes, including magnetic resistivity, thermal conduction, radiative transfer, partial ionization, and ambipolar diffusion [2,3,20-22]. Moreover, the numerical modeling of macrospicules convergence on two primary formation mechanisms: pulse- or shock-driven models [15,23,24] and reconnection-driven models [25-27]. Complementary observational inversions in He II 304 Å provide critical constraints, revealing non-ballistic shock-driven dynamics with typical velocities of 70-140 km s^{-1} and pronounced decelerations [10].

Despite substantial progress in the modeling of impulsively driven chromospheric jets, such jets have not yet been simulated using (MHD) equations coupled with a system of frequency and angle averaged radiation transport equations that independently evolve both the radiation energy density and the three components of the radiation flux. In this work, we present a numerical simulation of an impulsively driven jet in the solar atmosphere based on non-ideal MHD equations that incorporate highly anisotropic thermal conduction and empirical coronal heating. These equations are coupled to a radiation transport system that evolves both the radiation

energy density and the flux. The simulation focuses on the formation and evolution of a jet propagating through a region that includes the upper chromosphere and the solar corona, a medium characterized by low Planck-averaged absorption opacity and low Rosseland-averaged scattering opacity. In the low Planck mean opacity regime, radiative coupling via emission and absorption is weak, while in the low Rosseland mean opacity regime, photon diffusion is efficient and radiative transport is enhanced. In addition, we investigate whether the inclusion of radiation transport affects the morphology and dynamics of the chromospheric jet. This is motivated by previous models [15,19,28] that incorporated optically thin radiative cooling functions into the MHD equations and found that such effects can influence the dynamics of chromospheric jets with properties similar to those of spicules.

The paper is organized as follows. In Sec. 2, we describe the system of radiation MHD equations, including the relevant source and radiation terms. We also outline the solar atmospheric model, magnetic field configuration, radiation parameters, and the applied perturbation. In addition, we describe the details of the numerical methods used to solve the radiation MHD equations. In Sec. 3, we present the results of the numerical simulations. Section 4 discusses the impact of the radiation transport terms on jet dynamics, as well as the influence of source terms on the background solar atmosphere. Finally, Sec. 5 summarizes the conclusions and provides the final remarks.

2. Model and numerical methods

2.1. The system of radiation MHD equations

We consider a gravitationally stratified solar atmosphere described by a plasma coupled with the radiation field, for which a two-moment approach is adopted under the gray approximation. The resulting radiation (MHD) equations can be written in quasi-conservative form as

$$\frac{\partial \rho}{\partial t} + \nabla \cdot (\rho \mathbf{v}) = 0, \qquad (1)$$

$$\frac{\partial (\rho \mathbf{v})}{\partial t} + \nabla \cdot \left[\rho \mathbf{v} \otimes \mathbf{v} - \mathbf{B} \otimes \mathbf{B} \right. $$
$$\left. + \mathbf{I} \left(p + \frac{\mathbf{B}^2}{2} \right) \right]^T = \rho \mathbf{g} + \mathbf{G}, \quad (2)$$

$$\frac{\partial E_t}{\partial t} + \nabla \cdot \left[\left(\frac{\rho \mathbf{v}^2}{2} + \rho e + p \right) \mathbf{v} + c \mathbf{E} \times \mathbf{B} \right]$$
$$= \rho \mathbf{v} \cdot \mathbf{g} + c G^0 + \nabla \cdot \mathbf{F}_c + H, \quad (3)$$

$$\frac{\partial \mathbf{B}}{\partial t} + \nabla \times c \mathbf{E} = 0, \qquad (4)$$

$$\frac{1}{\hat{c}} \frac{\partial E_r}{\partial t} + \nabla \cdot \mathbf{F}_r = -G^0, \quad (5)$$

$$\frac{1}{\hat{c}} \frac{\partial \mathbf{F}_r}{\partial t} + \nabla \cdot \mathbb{P}_r = -\mathbf{G}, \qquad (6)$$

where ρ, p, $\mathbf{v}$, e, $\mathbf{B}$, and $\mathbf{E}$ are the plasma density, pressure, internal energy, velocity field, magnetic and electric fields. While E_r, $\mathbf{F}_r$, and $\mathbb{P}_r$ are the radiation energy, radiation flux, and radiation pressure tensor, respectively. There, $\mathbf{I}$ represents the identity matrix, c is the speed of light, and $\hat{c}$ is the reduced speed of light, which is introduced to reduce the overhead of the explicit integration of radiation transport terms. In sources terms, the equations include the gravitational acceleration vector $\mathbf{g} = [0, -g]$ with magnitude $g = 2.74 \times 10^4$ cm s^{-2}, the thermal conduction flux $\mathbf{F}_c$, the coronal heating function H, and the radiation interaction terms defined by $(G^0, \mathbf{G})$. In addition, E_t denotes the total energy density, *i.e.*, the sum of the internal, kinetic, and magnetic energy densities,

$$E_t = \rho e + \frac{\rho \mathbf{v}^2}{2} + \frac{\mathbf{B}^2}{2}, \qquad (7)$$

where a thermally ideal gas provides the closure $\rho e = \rho e(p, \rho)$, in terms of the following equation of state (EOS)

$$p = \frac{\rho k_B T}{m_u \mu}, \qquad (8)$$

where k_B is the Boltzmann constant, m_u is the atomic mass unit and μ is the mean molecular weight. This paper uses a value of $\mu = 0.6$, representing a fully ionized plasma, that is, a gas assumed about 92% of H and 8% of He.

The contribution from thermal conduction $\mathbf{F}_c$ is defined in terms of a flux-limited that smoothly varies between the classical and saturated thermal conduction regimes F_{class} and F_{sat}, respectively, that is:

$$\mathbf{F}_c = \frac{F_{\text{sat}}}{F_{\text{sat}} + |\mathbf{F}_{\text{class}}|} \mathbf{F}_{\text{class}}. \qquad (9)$$

In the above equation, the thermal conduction flux is highly anisotropic along the direction of the magnetic field lines, that is,

$$\mathbf{F}_{\text{class}} = \kappa_{\parallel} \frac{\mathbf{B}(\mathbf{B} \cdot \nabla T)}{|\mathbf{B}|}, \qquad (10)$$

where $\kappa_{\parallel} = 8 \times 10^{-7}$ erg s^{-1} cm^{-1} K^{-1}, which represents a typical value in the solar corona [29]. In the saturated flux limit, $F_{\text{sat}} = 5\phi\rho c_{\text{iso}}^3$, where c_{iso} is the isothermal speed of the sound and $\phi = 0.3$ is a free parameter that helps fix the value of F_{sat} [30].

The coronal heating function H that contributes as a source term to the total energy Eq. (3) helps to maintain a background solar corona against thermal conduction and radiative losses, as given in Ref. [29]

$$H = \max \left(\frac{c_0 * [(y - y_0)/h_0]^{-2/7}}{\exp[h_1/(y - y_1)] - 1}, 0 \right), \qquad (11)$$

where $c_0 = 0.01$ erg cm^{-3} s^{-1}, $y_0 = 1$ Mm, $h_0 = 5$ Mm, $y_1 = 2$ Mm and $h_1 = 3$ Mm. This background empirical heating function reaches its maximum value in about the transition region ~ 2.1 Mm, where it compensates for the cooling that radiation source terms could produce.

The components of the radiation pressure tensor, $\mathbb{P}_r$, are defined as a function of $(E_r, \mathbf{F}_r)$ through the closure of M1 introduced by [31], as

$$P^{ij} = E_r \left(\frac{1-\xi}{2} \delta^{ij} + \frac{3\xi - 1}{2} n^i n^j \right),$$
$$\xi = \frac{3 + 4f^2}{5 + 2\sqrt{4 - 3f^2}}, \tag{12}$$

where $\mathbf{n} = \mathbf{F}_r/|\mathbf{F}_r|$, $f = |\mathbf{F}_r|/E_r$, the sub-indexes i, j denote the spatial components of the radiation pressure tensor P^{ij}, and δ^{ij} is the Kronecker delta. The radiation-matter interaction terms $(G^0, \mathbf{G})$ are defined by boosting into the Eulerian frame their co-moving values, given by

$$(\tilde{G}^0, \tilde{\mathbf{G}})_{\text{comov}} = \rho[\kappa(\tilde{E}_r - a_R T^4), (\kappa + \sigma)\tilde{\mathbf{F}}_r]_{\text{comov}}. \tag{13}$$

In this equation, κ and σ are the frequency-averaged absorption and scattering coefficients, respectively, $a_R = 4\sigma_{\text{SB}}/c$ is the radiation constant, and T is the fluid temperature. The interaction terms in the laboratory frame that are the actual source terms in the equations are obtained by the following Lorentz transformation laws to the first order in $\beta = \mathbf{v}/c$:

$$G^0 = \tilde{G}^0 + \beta\tilde{\mathbf{G}}, \qquad \mathbf{G} = \tilde{\mathbf{G}} + \tilde{G}^0\beta. \tag{14}$$

Similarly, the radiation fields are transformed into the laboratory frame to the first order in β, as

$$E_r = \tilde{E}_r + 2\beta_i \tilde{F}_i$$
$$F_r^i = \tilde{F}_r^i + \beta^i \tilde{E}_r + \beta_j \tilde{P}_r^{ij}$$
$$P_r^{ij} = \tilde{P}_r^{ij} + \beta^i \tilde{F}^j + \beta^j \tilde{F}^i. \tag{15}$$

This implies the following expressions for the source terms implemented in the code:

$$G^0 = \rho\kappa(E_r - a_R T^4 - 2\beta \cdot \mathbf{F}_r)$$
$$+ \rho\chi\beta \cdot (\mathbf{F}_r - E_r\beta - \beta \cdot \mathbb{P}_r),$$
$$\mathbf{G} = \rho\kappa(E_r - a_R T^4 - 2\beta \cdot \mathbf{F}_r)\beta$$
$$+ \rho\chi(\mathbf{F}_r - E_r\beta - \beta \cdot \mathbb{P}_r), \tag{16}$$

where some $\mathcal{O}(\beta^2)$ terms are kept in order to recover the local thermal equilibrium (LTE) limit given by $\tilde{E}_r \rightarrow a_R T^4$ and $\tilde{F}_r \rightarrow \mathbf{0}$ when $\sigma, \kappa \rightarrow 0$ [32].

We can summarize the pros and cons of the closures employed in the radiation subsystem: i) The Eddington approximation assumes an isotropic radiation that works for optically thick regimes and provides a smooth transition from diffusion-like to free-streaming behavior. Nevertheless, it

can be inaccurate in optically thin regions and poor in highly anisotropic cases. ii) The flux-limited diffusion (FLD) closure introduces a flux limiter to handle transitions between optically thick and thin regimes, so it ensures a smooth transition from diffusion (optically thick) to free-streaming (optically thin) behavior and avoids unphysical superluminal fluxes. Nevertheless, it can be inaccurate in anisotropic fields and might lead to excessive diffusion. iii) The exact Eddington tensor solves the full radiative transfer equation (non-angular-averaged) to obtain the Eddington tensor, which makes it the most accurate of the three closures since it accounts for angular anisotropy. Also, it captures both optically thick and thin regimes without empirical flux limiters. Still, it is computationally expensive because it requires solving the full angular-dependent radiative transfer equation and becomes complex for multidimensional problems.

2.1.1. *The model of the solar atmosphere*

We assumed that the solar atmosphere was in hydrostatic equilibrium at the initial simulation time ($t = 0$ s). In particular, we choose the semi-empirical C7 model to describe the temperature field that covers the chromosphere and transition region [33], smoothly extended to the solar corona as, for example, [2]. In Fig. 1a), we show the equilibrium temperature, mass density, and gas pressure and profiles as functions of height y, where the steep gradient is discernible in the transition region $y \sim 2.1$ Mm, as indicated by a vertical black dashed line.

2.1.2. *The magnetic field*

The magnetic field $\mathbf{B}$ at the initial time is a 2D configuration that satisfies the force-free $(\nabla \times (\nabla \times \mathbf{B})) = \mathbf{0}$) and current-free $(\nabla \times \mathbf{B} = \mathbf{0})$ conditions, with the following components:

$$B_x(x, y) = \frac{-2S(x-a)(x-b)}{[(x-a)^2 + (y-b)^2]^2}, \tag{17}$$

$$B_y(x, y) = \frac{S(x-a)^2 - (x-b)^2}{[(x-a)^2 + (y-b)^2]^2}, \tag{18}$$

where S corresponds to the pole's magnetic field strength given in units of G Mm^2, and a and b are parameters that define the magnetic pole's location. In the right of Fig. 1, we show the magnetic field lines, where it is discernible that the field diverged at around $(x, y) = (5, 1.75)$ Mm. This inclined geometry of the magnetic field affects the jet's trajectory, which mainly follows the field lines, as will be shown later in this paper. This magnetic field configuration has already been used in numerical simulations of impulsively driven jets [15].

2.1.3. *The radiation parameters*

In this paper, we consider a plasma described by the non-ideal MHD coupled with the radiation transport equations, for which we adopt a gray approximation following a two-moment approach by imposing the M1 closure. This closure
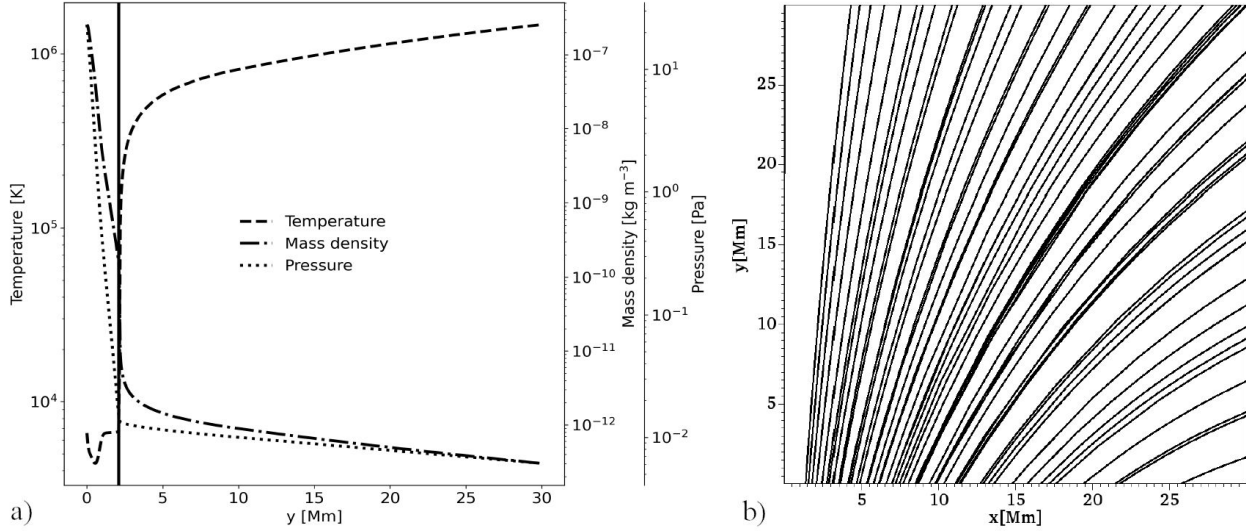
FIGURE 1. a) The logarithm of temperature in Kelvin (dashed line), the logarithm of mass density in kg m^{-3} (dash dot line), and the logarithm of gas pressure in Pa (dotted line) versus height, y in Mm, for the C7 equilibrium solar atmosphere model at the initial time ($t = 0$ s) of the simulation. The vertical dashed line (black) represents the location of the transition region at about $y \sim 2.1$ Mm. b) Representation of the magnetic field lines in the 2D domain at $t = 0$ s.

defines radiative transport in diffusion and free-streaming limits and can describe highly anisotropic radiation transport [34].

For radiation parameters, we chose the scattering opacity, $\sigma = 0.34$ cm^2 g^{-1}, the absorption opacity, $\kappa = 1 \times 10^{-6}$ cm^2 g^{-1}. The value of the scattering opacity corresponds to the electron scattering opacity, which dominates the corona's fully ionized, optically thin plasma. This opacity is given by:

$$\sigma = \frac{\sigma_T}{m_p}, \qquad (19)$$

where $\sigma_T = 6.65 \times 10^{-25}$ cm^2 is the Thomson scattering cross-section for free electrons, and $m_p = 1.67 \times 10^{-24}$ g is the proton mass. Assuming a fully ionized hydrogen plasma (where the electron number density is approximately equal to the proton number density), the opacity per gram of plasma is $\sigma \approx 0.398$ cm^2 g^{-1}. However, helium is also present in small fractions in the solar corona, which slightly reduces the free-electron fraction per unit mass. When typical coronal abundances are included (*e.g.* $He/H \approx 0.1$), the effective opacity is reduced to approximately 0.34 cm^2 g^{-1} [35,36]. For the value of the absorption opacity (10^{-6} cm^2 g^{-1}), in the solar corona, it is much lower than the scattering opacity because the primary absorption mechanisms (bound-free and free-free absorption) are weak at coronal temperatures ($T \sim 10^6$ K). The dominant source of absorption is free-free absorption (Bremsstrahlung), given by $\kappa \approx 10^{-6}$ cm^2 g^{-1} under typical coronal conditions [37,38].

At the initial time ($t = 0$ s) of the simulation, we set the radiation energy, $E_r = 2.2$ g cm^{-1} s^{-2} and the radial component of the radiation flux, $\mathbf{F}_r = F_{rr} = 2.1$ g cm^{-1} s^{-2}, which are typical values of the solar corona [39]. Also, at the initial simulation time, the solar corona is not in local thermodynamic equilibrium (LTE), since the radiation en-

ergy density does not follow the equation $a_R T^4$, and the radiation flux is not equal to zero. If we consider a system in LTE, the radiation flux in the solar corona is high ($\sim 10^{16}$ J m^{-3}), which dominates the plasma total energy density and produces instabilities in the numerical solution of the radiation MHD equations. Besides, physically, the solar corona does not necessarily radiate as an isotropic black body, since anisotropic effects, such as thermal conduction and coronal heating, should be added. Furthermore, the solar corona is optically thin for most photospheric radiation, and only negligible absorption or scattering of radiative energy by the gas occurs [39]. Even so, radiation scattering is important in the solar chromosphere. So, non-local thermodynamic equilibrium (NLTE) effects should be considered, since the ionization balance of hydrogen and helium is out of equilibrium, and assuming LTE to compute opacities is generally no longer accurate. In particular, the proper modeling of energy exchange must take into account the effects of NLTE, as implemented, for example, in Refs. [40-42].

We set the reduced value of the speed of light $\hat{c} = 0.1$, which has physical units of velocity and is part of the reduced speed of light approximation (RSLA). The need to use the RSLA is related to the ratio of the radiation propagation speed, c, to the maximum acoustic signal speed of the gas, which can be quite large in many astrophysical settings. Therefore, the ratio of the corresponding Courant-Friedrichs-Lewy (CFL) time steps for explicit integration of the gas and radiation transport subsystems, $\Delta t_{\text{gas}}/\Delta t_{\text{rad}} \sim c/v_{\text{max}}$, may be many orders of magnitude greater than 1. So an explicit scheme for the radiation subsystem can be rendered impractical by such a large ratio. Fortunately, in many situations we can reduce the signal propagation speed of the radiation fluid to some value $\hat{c} \ll c$, which in turn reduces the explicit time step ratio of gas to radiation to a computationally tractable

level, while preserving the essential dynamical behavior of the hydrodynamics (HD) or MHD system. This is the essence of RSLA, initially described by [43] and implemented by [44-46]. So in the case of this paper, we chose a value of $\hat{c} = 0.1$ that preserves the dynamic behavior of the MHD system and makes the evolution of the radiation subsystem computationally tractable. We also tested the simulation with four other different values of $\hat{c} = 10^{-2}$, 10^{-4}, 10^2 and 10^4. Yet, the results do not vary significantly regarding the jet's formation and evolution. The main effect of a specific choice of $\hat{c}$ is reflected in the computational time. For example, for values $\hat{c} = 10^2$ or $\hat{c} = 10^4$, the computational time increases considerably, making the calculations impractical for the scenario presented in this paper. Therefore, $\hat{c} = 10^{-1}$ is reasonable and appropriate in terms of computational cost. The choice of reduced speed of light, $\hat{c}$, was neither entirely arbitrary nor made solely for computational convenience. The rationale behind the (RSLA) is straightforward: since most astrophysical dynamics are modeled in the Newtonian limit (that is, the leading term in a Taylor expansion in powers of $1/c$), it is sufficient that the higher-order terms remain small compared to the leading one. For a system with characteristic velocity v, these terms scale as v/c. As long as $v/c \ll 1$, the Newtonian approximation holds. Therefore, the exact value of c is not critical, provided that $v \ll \hat{c}$, where $\hat{c}$ is the reduced speed of light, typically chosen as a fraction of the true speed of light (*e.g.*, $\hat{c} = 0.1c$, $0.5c$, or $0.7c$). In this study, the problem lies well within the Newtonian regime, as the characteristic velocity of the jet is on the order of tens of km s^{-1}, which is much lower than the adopted value of $\hat{c} = 0.1c$. This justifies the use of a reduced speed of light, which does not affect the physical dynamics but significantly reduces the computational cost. Thus, $\hat{c} = 0.1c$ is an appropriate and efficient choice for the simulations presented in this work.

Therefore, in this paper, the time-dependent formulation of radiative transfer has the following advantages: i) considering the evolution of the plasma variables coupled with the radiation energy density and radiation flux, and ii) adopting a gray approximation following a two-moment approach by imposing the M1 closure, which covers radiative transport in diffusion and free-streaming limits and can describe highly anisotropic radiation transport. However, the main disadvantages are: i) neglecting the effects of radiation scattering in the solar chromosphere and the NLTE effects, and ii) simplification of the treatment of the radiation field by considering the frequency-integrated zeroth- and first-order angular moments of the radiative transfer equation.

2.1.4. Perturbation

To excite jet formation, we perturb the initial background state of the solar atmosphere by a simple localized Gaussian pulse set in the vertical component of velocity, which is a standard procedure for triggering jets [15,23,47]. Specif-

ically, the velocity pulse is

$$v_y(x, y) = A_v \exp\left(-\frac{(x-x_0)^2 + (y-y_0)^2}{w^2}\right). \quad (20)$$

In the above expression, A_v defines the amplitude of the pulse, (x_0, y_0) is the initial position of the pulse, and w is its width. In this paper, we set and hold $A_v = 100$ km s^{-1}, $x_0 = 5$ Mm, $y_0 = 1.75$ Mm, and $w = 0.2$ Mm. These values are typical for exciting jets that resemble some macrospicule characteristics in adiabatic and non-adiabatic numerical MHD simulations [15,23].

2.2. Numerical methods

We numerically solve Eqs. (1)-(6) using version 4.4-patch3 of the PLUTO code [48], which incorporates a radiation module based on the two-moment radiation hydrodynamic scheme described in Ref. [34]. The simulations employ a Courant-Friedrichs-Lewy (CFL) number of 0.4 and use a second-order total variation-diminishing (TVD) Runge-Kutta time integrator. For the integration of the MHD equations, we adopt the approximate Harten-Lax-van Leer discontinuities (HLLD) Riemann solver [49], while the radiation transport equations are solved using the Harten-Lax-van Leer contact solver (HLLC) [50]. In both cases, a linear reconstruction of the primitive variables is applied, combined with the minmod slope limiter.

To control the numerical violation of the divergence-free condition ($\nabla \cdot \mathbf{B} = 0$), we adopt the constrained transport method (CT), which computes the electric field $\mathbf{E}$ using a simple arithmetic averaging scheme [51]. This approach ensures that the solenoidal constraint on the magnetic field is preserved to machine precision throughout the numerical evolution. The integration of the radiation transport step follows the methods implemented in [52]. Specifically, Eqs. (5) and (6) are advanced in time using Implicit-Explicit Runge-Kutta (IMEX-RK) schemes [53]. In these schemes, flux terms are treated explicitly, while radiation-matter interaction terms are implicitly integrated. PLUTO provides two IMEX schemes for this purpose: the IMEX-SSP2(2,2,2) method [54] and the IMEX1 scheme introduced by [52]. The IMEX-SSP2(2,2,2) method is a two-stage second-order scheme with strong stability preserving properties (SSP), widely used for stiff hyperbolic-parabolic systems. In contrast, the IMEX1 scheme is a first-order formulation tailored for MHD with parabolic terms, designed to efficiently handle stiff dissipative terms while maintaining simplicity and robustness. Thermal conduction is evolved separately from the advection terms via operator splitting, using the super-time-stepping (STS) method [55]. This approach is particularly well-suited for efficiently handling the highly parabolic nature of the thermal conduction term in the MHD equations. Lastly, the empirical coronal heating term in the energy Eq. (3) is explicitly integrated in time, without imposing additional constraints on the time step.
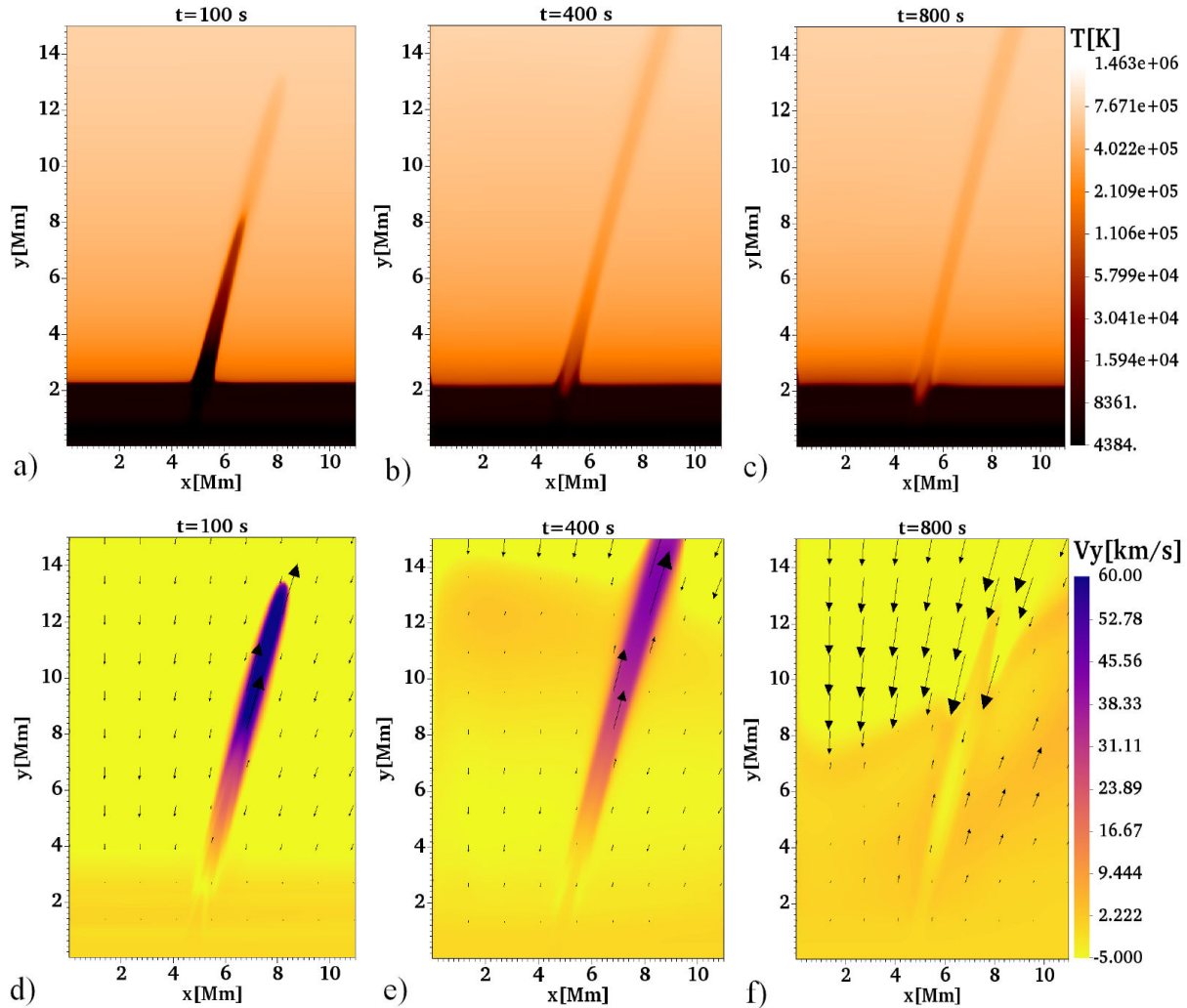
FIGURE 2. Top row: spatial profiles of temperature (in Kelvin) at a) $t = 100$ s, b) $t = 400$ s, and c) $t = 800$ s. Bottom row: Vertical component of velocity V_y in km s^{-1} with velocity vector field at the exact three times as temperature.

The simulation is carried out in a two-dimensional Cartesian domain with spatial coordinates $x \in [0, 30]$ Mm and $y \in [0, 30]$ Mm, discretized on a uniform grid of 1200×1200 cells. This corresponds to an effective spatial resolution of 25 km in both directions. In this setup, the lower boundary at $y = 0$ Mm corresponds to the base of the photosphere. For (MHD) variables, we impose fixed-time boundary conditions, maintaining all quantities at their equilibrium values along the edges of the domain at $x = 0$, $x = 30$ Mm, $y = 0$, and $y = 30$ Mm. In contrast, for radiation variables, namely the radiation energy density E_r and the radiation flux vector $\mathbf{F}_r$, we apply the outflow boundary conditions at the four domain boundaries. These conditions allow radiation to freely exit the computational domain, ensuring a physically consistent treatment of radiative transport across the boundaries.

3. Results of numerical simulations

In Fig. 2, we show snapshots of the spatial profiles of plasma temperature in Kelvin in the top panels and the vertical com-

ponent of the velocity in km s^{-1} with the vector velocity field overplotted in the bottom panels. Specifically, on the temperature map at $t = 100$ s, we observe the formation of a collimated plasma structure that resembles a jet that reaches a height of about 8 Mm. This jet reaches a maximum temperature of approximately 8×10^4 K and also shows at its head the development of a collimated hot plasma structure ($\sim 2 \times 10^5$ K) that propagates upward. At $t = 400$ s, the jet becomes smaller (~ 1.5 Mm in length) compared to its precedent at $t = 100$ s; it also exhibits a double-thread structure at the top of it, which is a typical feature of solar spicules [56,57]. At $t = 800$ s, the temperature map shows that the jet practically diffuses and that only its tiny double thread remains over the transition region (~ 2.1 Mm) and the upper chromosphere (~ 3 Mm). In the bottom row of Fig. 2, we display vertical velocity maps v_y with the vector velocity field showing consistency with the temperature behavior described above. In particular, at $t = 100$ s, the jet reaches a vertical velocity of about 30 km s^{-1}, while the plasma at the top of it reaches a maximum high vertical velocity of around
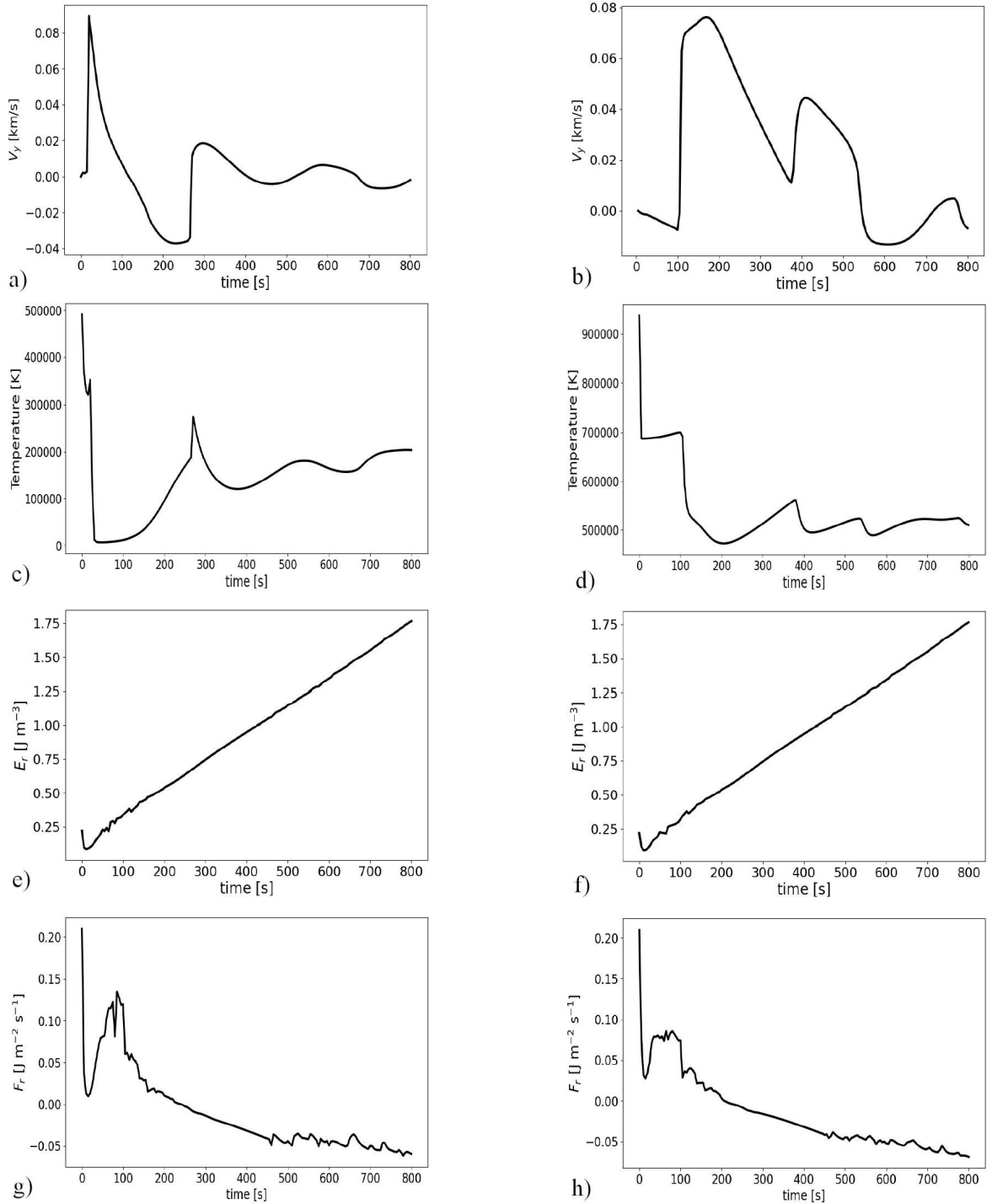
FIGURE 3. Time signatures of the vertical velocity, v_y, in km s^{-1} a)-b), the temperature, in Kelvin c)-d), the radiation energy density, E_r, in J m^{-3} e)-f), and the radial component of the radiation flux, F_r, in J m^{-2} s^{-1} g)-h), collected at the point $x = 5.6, y = 4$ Mm (left panels) and $x = 8.5, y = 14$ Mm (right panels).

60 km s^{-1}). This high-velocity is associated with a shock front generated by the perturbation that moves from a cooler (denser) medium to a hotter (less dense) medium into the solar corona. This is a typical behavior obtained in numerical simulations of impulsively driven jets [47]. However, at $t = 400$ s, the plasma associated with the shock reaches the top boundary at $y = 30$ Mm. At $t = 800$ s, the vertical velocity is predominantly negative, indicating the jet diffusion. Interestingly, radiative terms in the momentum and total energy density equations and their coupling with the plasma

could generate this negative plasma-flow motion. This result, in turn, is consistent with the effect of the optically thin radiative losses, as shown in Ref. [15].

In Fig. 3, we show the time signatures of the vertical velocity v_y (km s^{-1}), temperature (K), radiation energy density E_{nr} (J m^{-3}) and the radial component of the radiation flux F_r (J m^{-2} s^{-1}) at the detection points $(x = 5.6, y = 4)$ Mm (left panels) and $(x = 8.5, y = 14)$ Mm (right panels). In this paper, a time signature refers to the temporal evolution of a physical quantity at a fixed spatial location, used to identify the characteristic temporal behavior or periodicity in the time series of the plasma and radiation variables described above. In these time signatures, the point $(x = 5.6, y = 4)$ Mm lies within the jet and $(x = 8.5, y = 14)$ Mm is where the shock passes. In Fig. 3a), we show the time signatures of v_y at $(x = 5.6, y = 4)$ Mm, where the vertical velocity inside the jet reaches a maximum value of about 90 km s^{-1} around 20 s after the simulation starts. After this stage, the vertical velocity becomes negative up to around -40 km s^{-1} at $t = 250$ s. Following this behavior, the velocity increases again, with values of 20 km s^{-1}. From around $t = 350$ s onward, the vertical velocity within the jet remains negative, indicating diffusion. In Fig. 3b), the time signatures of the vertical velocity collected at the point $(x = 8.5, y = 14)$ Mm indicate that the shock moves fast and reaches a maximum velocity of around 80 km s^{-1} at approximately $t = 180$ s. After that time, the vertical velocity of the shock decreases to a value near 18 km s^{-1} at about $t = 360$ s. Later, the vertical velocity increases again to a value of around 45 km s^{-1}. Nonetheless, after 400 s, the vertical velocity of the shock decreases and reaches negative values. This behavior indicates that plasma inside the shock moves downwards from the solar corona to the transition region and chromosphere. In Fig. 3c), the time signatures of temperature measured at the detection point $(x = 5.6, y = 4)$ Mm show that the temperature inside the jet rapidly decreases at the start of the simulation ($t \approx 50$ s). Later, the temperature increased to an order of magnitude of 10^5 K close to 300 s. From 300 to 800 s, the temperature varies slightly and remains close to 2×10^5 K. In Fig. 3d), the time signatures of the temperature collected at $(x = 8.5, y = 14)$ Mm indicate that the temperature inside

the shock is in the range of $7 \times 10^5 - 9 \times 10^5$ K in the first 100 s of simulation. After that time, the temperature of the shock decreases to a value close to 3×10^5 K, at $t = 200$ s. After 200 s, the temperature slightly varies around 5×10^5 K to reach the final simulation time $t = 800$ s.

In Figs. 3e) and 3f), we show the time signatures of the radiation energy density collected at two detection points described above. In these time histories, we identify a linear growth of the radiation energy density inside the jet and within the shock wave during the total simulation time. In particular, the radiation energy density reaches a maximum value of around 1.75 J m^{-3} at both detection points. Finally, in Figs. 3g) and 3h), that is, at the bottom, the time signatures of the radial component of the radiation flux show the opposite behavior to the radiation energy density. Remarkably, the radiation flux decreases; this behavior could be associated with the radiation energy loss processes at the solar corona, which, in turn, might be related to an optically thin radiative cooling process.

To identify the dynamics of the plasma associated with the jet and shock, in Fig. 4, we show distance-time diagrams of the vertical velocity v_y in km s^{-1} and the logarithm of the mass density ρ in kg m^{-3} measured in a line of about 8.15 Mm in length that goes along with the jet, similar to the analysis performed in Ref. [15]. For example, on the left of Fig. 4, the temporal and spatial evolution of the vertical velocity along the jet schematizes the generation of a shock wave combined with a contact wave at the beginning of the jet formation. In the right panel of Fig. 4, we depict the behavior of the mass density along the jet, which shows that the jet reaches a height of about 8 Mm at $t \approx 100$ s. It is also evident that there is periodic behavior in the jet dynamic, and it follows a typical parabolic path with a period of around 300 s, which could be related to a chromospheric jet such as spicules [58].

In summary, the numerical results described in the previous paragraphs reveal that the impulsively driven chromospheric jet rapidly develops into a collimated plasma structure reaching a height of about 8 Mm, with temperatures up to 8×10^4 K and a hotter leading edge of $\sim 2 \times 10^5$ K. At
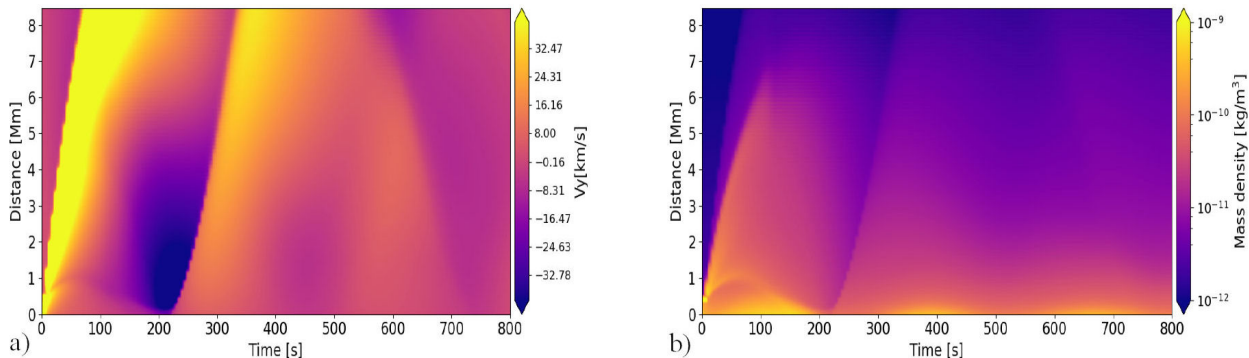

FIGURE 4. a) Distance-time diagrams of the vertical velocity v_y, in km s^{-1}, and b) the logarithm of mass density, ρ, in kg m^{-3}.

late simulation times, the jet exhibits a characteristic double-thread morphology and eventually dissipates back into the lower atmosphere. In addition, vertical velocity attains values of ~ 30 km s^{-1} within the jet and up to ~ 60 km s^{-1} at the associated shock front, with time signatures at fixed locations indicating peak velocities close to 90 km s^{-1} before declining and becoming negative as the structure decays. The temperature inside the jet stabilizes around 2×10^5 K, while in the shock region it decreases from 9×10^5 K to around 3×10^5 K during simulation. Likewise, the radiation energy density increases linearly to ~ 1.75 J m^{-3}, whereas the radiation flux decreases, consistent with optically thin radiative cooling. The distance-time diagrams confirm a parabolic trajectory with a period of ~ 300 s, reproducing the classical spicule-like dynamics prior to the final dissipation of the jet.

Overall, the results of this section demonstrate that although the simulated jet reproduces some characteristics similar to classical spicules, its rapid fading is strongly influenced by radiative processes. In particular, the explicit evolution of the radiation energy density and flux through the two-moment transport equations reveals that radiation acts as an efficient optically thin cooling mechanism in the corona. This mechanism induces downward flows and thermal energy loss, thereby limiting the height, duration, and energy content of the jet. Consequently, the present findings not only agree with previous studies [15,19] employing empirical radiative loss functions, but also emphasize that a self-consistent treatment of radiation transport is crucial to capture the dissipation and evolution of macrospicule-like events.

4. Discussion

4.1. Effects of the radiation transport terms on the jet

To show whether the radiation transport terms affect the formation, morphology, and evolution of the jet, in Fig. 5, we display maps of the radiation energy density E_r and the magnitude of the radiation flux $|\mathbf{F}_r|$ with the vector velocity field and a density contour (in red) of 10^{-14} kg m^{-3} at three representative times, $t = 100, 400, 800$ s. In addition, to schematize the dominant density energy in the evolution of the jet, at the bottom of Fig. 5, we depict spatial profiles of the ratio E_r/e_{int} at the same times as E_r and $|\mathbf{F}_r|$. For example, in the upper panels of Fig. 5 at the three times, the radiation energy density maps E_r show a constant value in the region that covers the jet structure, which is delimited by the mass density contour in red. In the middle panels of Fig. 5, we distinguish that the magnitude of the radiation flux $|\mathbf{F}_r|$ is low in the chromosphere, but increases at the corona. Despite this, the radiation flux remains constant in the region where the jet develops and does not shape the jet morphology either. In the bottom panels of Fig. 5, the maps of the ratio E_r/e_{int} show that e_{int} dominates the radiation energy density E_r in the corona, but in the chromosphere and transition region the radiation energy density E_r is more significant than e_{int}. That

said, the internal energy density is what gets the shape and morphology of the jet, since it is directly associated with the plasma variables, such as mass density and velocity. In all of the panels, the velocity vector field shows consistency in the jet's dynamics. Evidently, a strong negative flow at the solar corona ultimately diffuses the jet. Although the radiation transport variables do not get the shape and morphology of the jet, both affect their evolution, since they permeate the medium where the jet forms and propagates. In Appendix A, we show representative results of a basic test that show the behavior of the radiative version of the MHD blast wave considering the limits of an optically thick medium and an optically thin medium. This test illustrates how plasma fluid depends on the evolution of radiation transport equations in a more basic scenario than the study here.

The simulation results indicate that radiation transport contributes to the evolution of chromospheric jets, which is consistent with previous studies that have shown the key role of radiative cooling in shaping their properties [15,19,28]. Radiative losses influence the temperature, density, and velocity of the chromospheric jet by extracting thermal energy from the plasma, modifying pressure gradients, and the overall energy budget. This process, in turn, governs the height, lifetime, and morphology of the jets.

Furthermore, the results presented in this work exhibit notable similarities with those reported by [15,19], while also introducing a novel approach to modeling chromospheric jets. In Ref. [19], one-dimensional simulations assuming a pure hydrogen plasma with optically thin radiative losses and NLTE hydrogen ionization demonstrated that a substantial fraction of the injected energy is redistributed to ionization rather than heating. This redistribution leads to spicules that are shorter and weaker in their model. However, it is important to note that those simulations were performed in a hydrogen-only plasma, whereas in our study we adopt a more realistic composition of hydrogen and helium, corresponding to a mean molecular weight of $\mu = 0.6$. The inclusion of helium modifies the thermodynamic response of the plasma by changing the specific heat, sound speed, and energy partition, which, in turn, can affect the jet's evolution and energy transfer. Therefore, our comparison with hydrogen-only studies should be interpreted qualitatively: while the specific thermodynamic response may differ, the general conclusion that radiative processes redistribute energy away from heating and into ionization remains valid. In this context, the present work extends earlier findings by explicitly solving the two-moment radiation transport equations, thereby capturing the optically thin radiative cooling in a self-consistent way for a more realistic solar composition.

4.2. Effects of the source terms on the background solar atmosphere model

To qualitatively and quantitatively measure whether the temperature of the background atmosphere varies without the vertical velocity perturbation, but considering the non-ideal
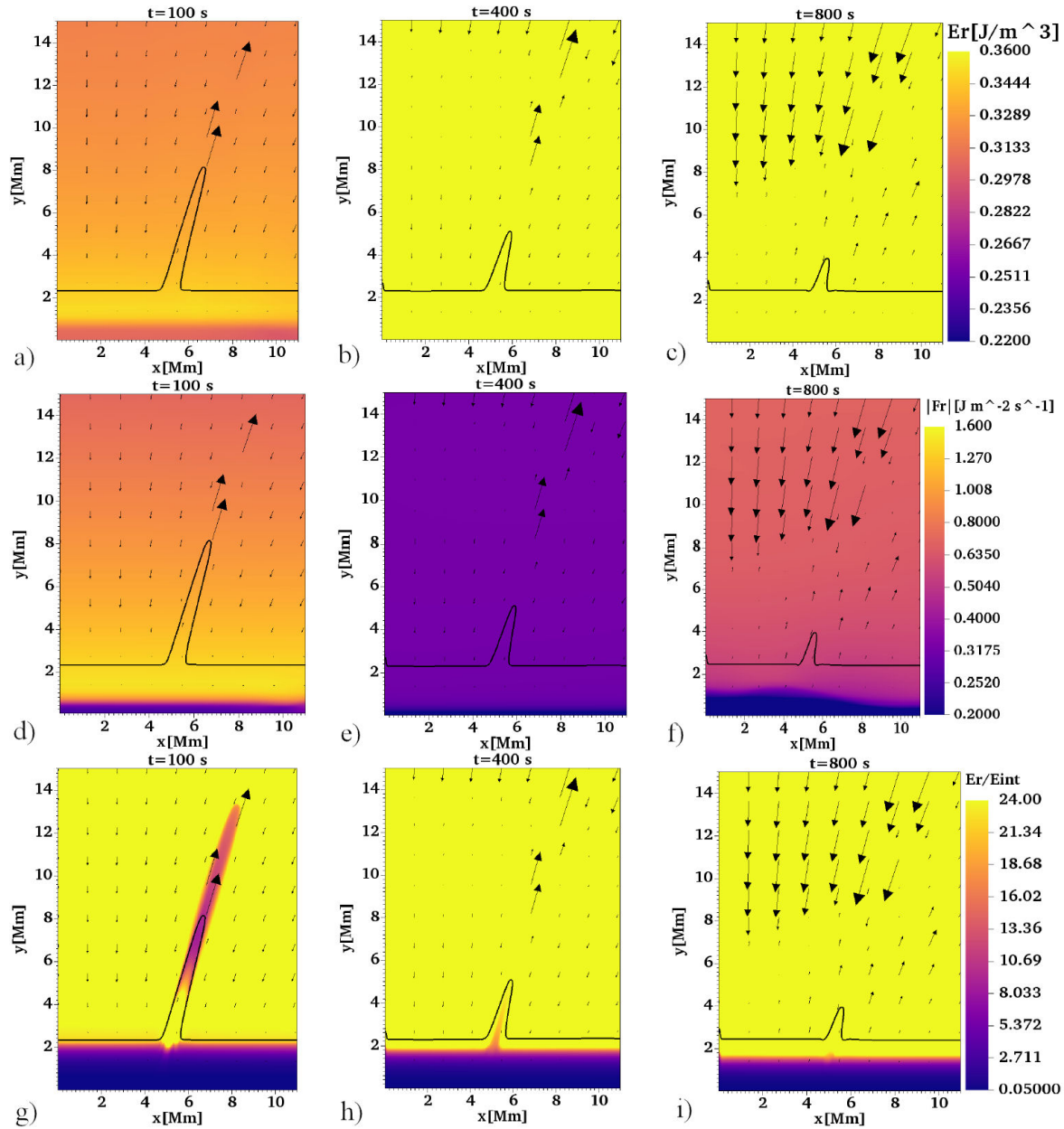
FIGURE 5. (Top) Spatial profiles of radiation energy density E_r (in J m^{-3}), magnitude of the radiation flux $|\mathbf{F_r}|$ in J m^{-2} s^{-1} (middle), and the ratio E_r/e_{int} (bottom), at the times a) $t = 100$ s, b) $t = 400$ s, and c) $t = 800$ s. The vectors (in black) represent the velocity vector field, and the contour (in black) represents a constant mass density of 10^{-14} kg m^{-3}.

effects such as thermal conduction, coronal heating, and radiation, in Fig. 6, we display 1D cuts of the temperature as a function of the height y at five different times ($t = 0, 100, 200, 400, 800$ s). We also calculate the relative error from point to point between the temperature values at the initial time ($t = 0$ s) compared to the temperature values at $t = 400$ s and $t = 800$ s and the relative error between the temperatures values at $t = 400$ s and $t = 800$ s. For example, on the left of Fig. 6, we depict the 1D temperature profiles on a vertical line traced from $y = 0$ Mm to $y = 30$ Mm, which is located in the middle of the numerical 2D domain, that is, at $x = 15$ Mm. We can see that the temperature decreases slightly from time $t = 100$ s to the final time

$t = 800$ s. Despite the decrease in the background temperature profile, the variations are not substantial, and the solar corona temperature remains globally stable against the effect of the source terms. Furthermore, to quantitatively show the errors between the 1D temperature cuts, on the right of Fig. 6, we show the results of the estimation of the relative error calculated according to the following expression,

$$\text{Relative error} = \left| \frac{T_i - T_0}{T_0} \right|, \tag{21}$$

where T_0 is the temperature profile at $t = 0$ s, and T_i with $i = 1, 2$ are the temperature profiles at $t = 400$ s and
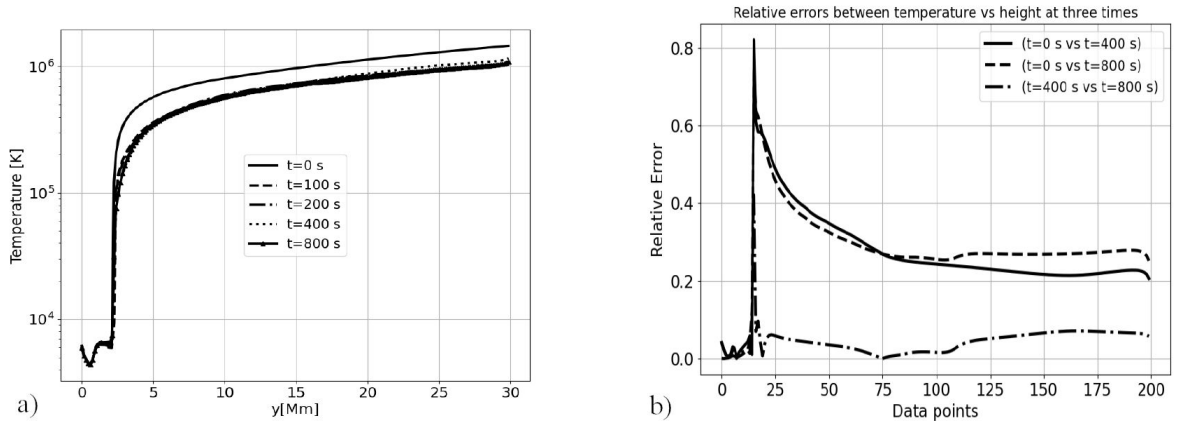
FIGURE 6. a) 1D cuts corresponding to five times ($t = 0, 100, 200, 400$ and 800 s) of the solar background model's plasma temperature in Kelvin as a function of height y in Mm. b) The relative error between temperature values for three times $t = 0, 400$, and 800 s.

$t = 800$ s, respectively. Therefore, in that plot, we observe a high relative error between T_0 and T_1 for some data points. This high value is also reached by the relative error between T_0 and T_2, and T_1 and T_2. Although this is a high value of the relative error, in the three curves, the relative error decreases and tends to a low value. The lowest relative error is between T_1 and T_2, while the highest relative error is achieved between T_0 and T_1, but it is of the same order as T_0 and T_2. The high value of the relative error in the three comparisons is due to the values at the transition region, since a sharp gradient could make a point-to-point comparison vary significantly.

5. Conclusions and final comments

The main objective of this paper was to study the formation and evolution of an impulsively driven chromospheric jet that resembles some spicule features using a 2D non-ideal radiation MHD numerical simulation. Specifically, we model the solar atmosphere and the jet as a plasma that follows the MHD equations coupled to a system of frequency- and angle-averaged radiation transport equations that include the evolution of the radiation energy flux and the radiation flux components. To trigger the formation of the jet, we perturb the solar atmosphere with a localized Gaussian pulse in the vertical velocity, set at the solar chromosphere ($y = 1.75$ Mm). In addition, we initially considered a solar atmosphere in (NLTE) by setting characteristic low values of the Planck-averaged absorption opacity ($\kappa = 1 \times 10^{-6}$ cm^2 g^{-1}) and the Rosseland-averaged scattering opacity ($\sigma = 0.34$ cm^2 g^{-1}) corresponding to an optically thin medium such as the solar corona.

Based on the results of the numerical simulation, we observe classical features on the mechanism of jet formation reported in various numerical MHD simulations of impulsively driven jets [15,17,23,47], where the mechanism can be explained in terms of the following physics. The localized pulse rapidly transforms into shocks that propagate upward and generate the collimated plasma structure with some features of a solar spicule. In addition, the pulse also ex-

cites a non-linear wake in the chromosphere, which leads to quasi-periodic secondary shocks, which in turn lift the chromospheric plasma upward and create quasi-periodic jets in the solar corona. In summary, the chromospheric jet modeled in this study exhibits some characteristics that resemble observed macrospicules, while also presenting differences. In terms of height, the simulated jet reaches a maximum vertical extent of approximately 8 Mm above the transition region, placing it at the lower limit of the observed macrospicule height range, which spans from 7 to 70 Mm above the solar limb [59]. The width of the simulated jet, approximately 1 Mm, is also consistent with the typical macrospicule widths, which are generally around 3 Mm. However, the maximum vertical velocity reached in the simulation, about 40 km s^{-1}, falls below the lower bound of the observed velocity range for macrospicules, which lies between 70 and 140 km s^{-1} [10]. This suggests that the simulated jet corresponds to a relatively low-energy event. Similarly, the maximum temperature attained in the simulation, approximately 8×10^4 K, is lower than the typical macrospicule temperature range of $(1-2) \times 10^5$ K [60]. Despite these differences, the simulation successfully reproduces several dynamical features commonly associated with macrospicules, including shock formation, double-thread structures, and jet dissipation. The inclusion of radiation transport equations that evolve both the radiation energy density and flux demonstrates that radiation acts as an efficient cooling mechanism in the optically thin corona. This cooling facilitates downward flows and contributes to the eventual dissipation of the jet. The radiative behavior observed in this study is consistent with the results of earlier models employing empirical radiative loss functions [15], reinforcing the conclusion that radiative losses, whether empirically prescribed or self-consistently computed by radiation transport, play a central role in limiting the height and energy content of macrospicules.

Concerning the effects of the radiation transport term on the chromospheric jet, we identify that either the radiation energy density or radiation flux determines the morphology of the jet, but both variables permeate the solar atmospheric

environment where the jet propagates. In particular, the radiation energy density distributes more homogeneously than radiation energy flux over the solar atmosphere domain without significantly affecting the background solar model. Interestingly, the radiation energy density and radiation flux at the solar corona lead to a negative flow that diffuses the jet and makes it tiny. This result is consistent with the result obtained in Ref. [15], where the authors explored the effects of radiative cooling on the formation and evolution of solar jets with some macrospicule features. In that paper, the authors found that radiative cooling produced a negative flow that dissipated the jet, making it short and cold. Such a study considers radiative cooling represented by an optically thin radiative loss function computed according to the CHIANTI code, which is an atomic database and software package used to model emission lines and continua from hot and optically thin astrophysical plasmas [61]. The current study did not consider the optically thin radiative loss function as a source term in the total energy density equation. Instead, we con-

sidered the coupling system of the MHD equations with the radiation transport equations that had never been attempted before. We found that in an optically thin region such as the solar corona, where the scattering and absorption opacities are low, the radiation terms act as an optically thin radiative loss mechanism. This result is interesting since it tells us that the more appropriate treatment of the coupling between matter and radiation in the context of spicule simulations could be the solution of the MHD equations with radiative transfer, which includes the optically thick radiation and the numerical recipes for the radiative transfer similar to what has been done in, for example, [20,21,42]. Finally, in this paper, it is the first time so far that the evolution of the radiative energy density and radiative flux in the formation and evolution of an impulsively driven chromospheric jet has been shown and deserves attention to explore potential applications in future studies in optically thick regions such as solar convection phenomena.
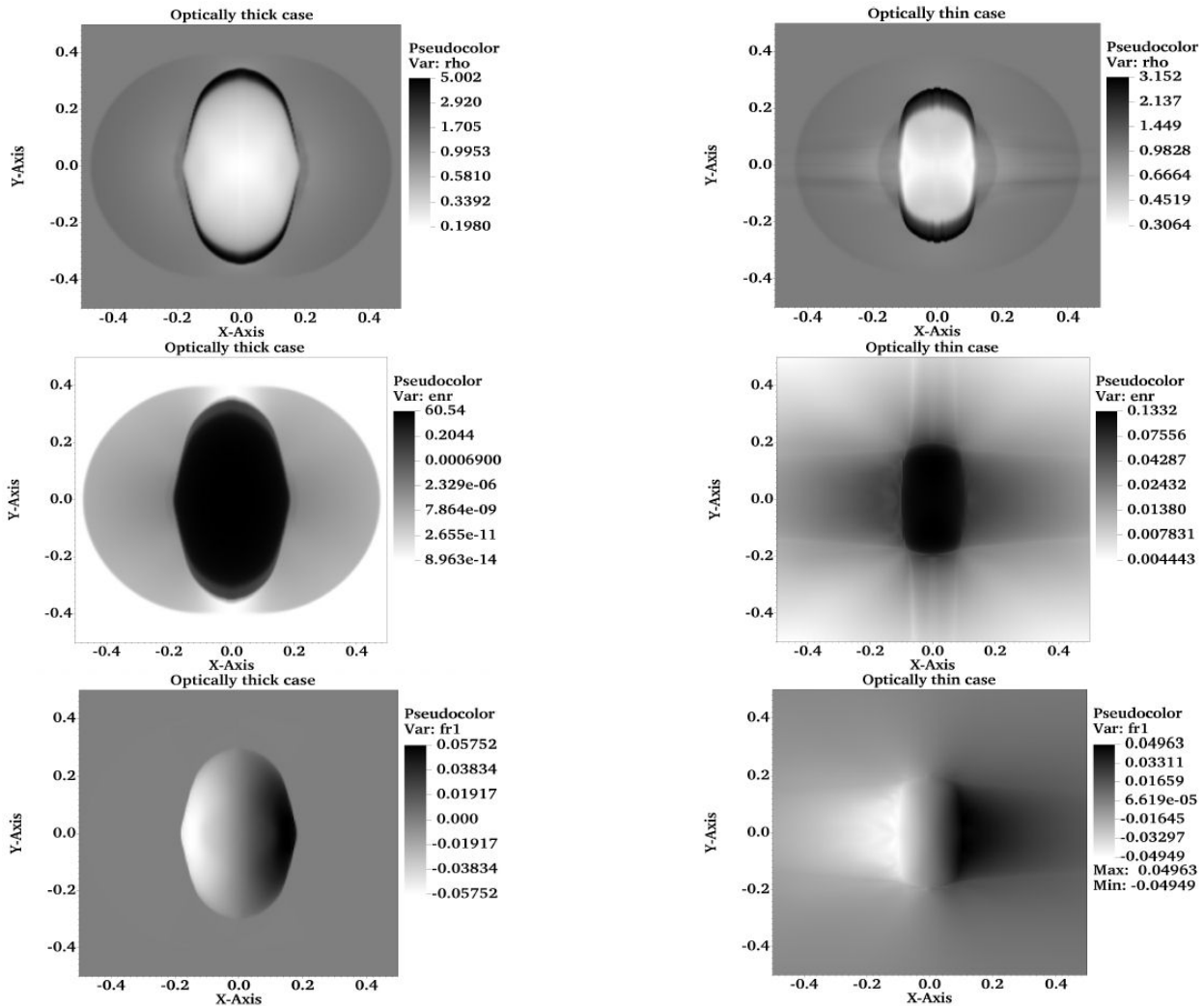

FIGURE 7. Spatial profiles of the mass density (top), radiation energy density (middle), and radiation energy flux (bottom) correspond to the 2D radiative MHD blast wave test for the optically thick case (left) and optically thin case (right). All the plots are at $t = 0.01$ in code units.

A Dynamics of the plasma and the radiation field in a basic MHD test

To illustrate how the plasma behaves while coupling with the radiation field, in this Appendix A, we show representative results of the radiation version of the MHD blast wave test for optically thick and optically thin cases. In the ideal MHD equations, the blast wave measures the ability of the numerical algorithms implemented in the PLUTO code to handle strong waves propagating in highly magnetized environments. It is also helpful to test the code to control non-physical densities or pressures by adequately controlling the divergence-free condition. The 2D radiative version of the MHD blast wave consists of the same setup for the plasma variables as for the ideal MHD test. However, it includes initial conditions for the radiation energy density and the radiation flux (1-6), but without dissipative terms in a 2D Cartesian domain.

In Fig. 7, we show maps of the mass density (top), radiation energy density (middle), and the $x-$component of the radiation flux (bottom) for the optically thick (left) and optically thin (right) scenarios. For the optically thick case, that is, for a high absorption opacity ($\kappa = 10^4$), we see the typical behavior of the mass density, similar to the blast wave in the ideal MHD approximation. However, interestingly, the radiation energy density shows a morphology similar to that of the mass density, and it also contributes to the acceleration of the MHD shock wave. Furthermore, the $x-$ component of the radiation flux also couples with the evolution of the plasma mass density. This behavior implies that the plasma is predominantly coupled with the radiation field in the optically thick scenario. On the other hand, in the right panels of Fig. 7, we depict the maps for the optically thin scenario, that is, for a low absorption opacity ($\kappa = 1$). In these panels, it is clear that the morphology of the mass density is different from that in the optically thick case. Precisely, the plasma density moves slowly at the front shock, and the radiation energy density is low, which does not significantly affect the plasma motion. In addition, the map of the $x-$ component of the radiation flux schematizes the propagation opposite to the intense shock front.

Acknowledgments

1. K. Shibata *et al.,* Chromospheric Anemone Jets as Evidence of Ubiquitous Reconnection, *Science* **318** (2007) 1591, https://doi.org/10.1126/science.1146708

2. J. J. González-Avilés, F. S. Guzmán, and V. Fedun, JET Formation in Solar Atmosphere Due to Magnetic Reconnection, *The Astrophysical Journal* (2017) 10, https://dx.doi.org/10.3847/1538-4357/836/1/24

3. J. J. González-Avilés *et al.*, I. Jet Formation and Evolution Due to 3D Magnetic Reconnection, *The Astrophysical Journal* **856** (2018) 176, https://dx.doi.org/10.3847/1538-4357/aab36f

4. J. M. Beckers, Solar Spicules, *Annual Review of Astronomy and Astrophysics* **10** (1972) 73, https://doi.org/10.1146/annurev.aa.10.090172.000445

5. J. M. Beckers, Solar Spicules (Invited Review Paper), *Sol Phys* **3** (1968) 367, https://doi.org/10.1007/BF00171614

6. T. V. Zaqarashvili and R. Erdélyi, Oscillations and Waves in Solar Spicules, *Space Sci Rev* **149** (2009) 355, https://doi.org/10.1007/s11214-009-9549-y

7. B. De Pontieu *et al.*, A Tale of Two Spicules: The Impact of Spicules on the Magnetic Chromosphere, *Publications of the Astronomical Society of Japan* **59** (2007) S655, https://doi.org/10.1093/pasj/59.sp3.S655

8. D. H. Sekse, L. Rouppe van der Voort, and B. De Pontieu, Statistical properties of the Disk Counterparts of Type II Spicules from simultaneous observations of RBEs in Ca II 8542 and Hα, *The Astrophysical Journal* **752** (2012) 108, https://doi.org/10.1088/0004-637X/752/2/108

9. J. D. Bohlin *et al.*, A newly observed solar feature: macrospicules in He II 304 Å, *The Astrophysical Journal Letters* **197** (1975) L133, https://doi.org/10.1086/181794

10. I. P. Loboda and S. A. Bogachev, What is a Macrospicule?, *The Astrophysical Journal* **871** (2019) 230, https://doi.org/10.3847/1538-4357/aafa7a

11. Murawski, K. and Zaqarashvili, T. V., Numerical simulations of spicule formation in the solar atmosphere, *Astronomy and Astrophysics* **519** (2010) A8, https://doi.org/10.1051/0004-6361/201014128

12. Murawski, K., Srivastava, A. K., and Zaqarashvili, T. V., Numerical simulations of solar macrospicules, *Astronomy and Astrophysics* **535** (2011) A58, https://doi.org/10.1051/0004-6361/201117589

13. B. Kuzma *et al.*, Numerical simulations of solar spicules: Adiabatic and non-adiabatic studies, *Astronomy and Astrophysics* **597** (2017) A133, https://doi.org/10.1051/0004-6361/201628747

14. B. Singh, K. Sharma, and A. K. Srivastava, On modelling the kinematics and evolutionary properties of pressure-pulse-driven impulsive solar jets, *Annales Geo physicae 37 (2019)* 891, https://doi.org/10.5194/angeo-37-891-2019

15. J. J. González-Avilés *et al.*, Numerical simulations of macrospicule jets under energy imbalance conditions in the solar atmosphere, *Monthly Notices of the Royal Astronomical Society* **505** (2021) 50, https://doi.org/10.1093/mnras/stab1261

16. J. J. González-Avilés, K. Murawski, and T. V. Za qarashvili, Numerical simulations of a two-fluid jet at a magnetic null point in a solar arcade, *Monthly Notices of the Royal Astronomical Society* **515** (2022) 5094, https://doi.org/10.1093/mnras/stac2032

17. A. K. Srivastava *et al.*, Impulsive origin of solar spicule-like jets, *European Physical Journal Plus* **138** (2023) 209, https://doi.org/10.1140/epjp/s13360-023-03833-5

18. A. C. Sterling and J. V. Hollweg, The Rebound Shock Model for Solar Spicules: Dynamics at Long Times, *The Astrophysical Journal* **327** (1988) 950, https://doi.org/10.1086/166252

19. A. C. Sterling and J. T. Mariska, Numerical Simulations of the Rebound Shock Model for Solar Spicules, *The Astrophysical Journal* **349** (1990) 647, https://doi.org/10.1086/168352

20. J. Martínez-Sykora *et al.*, Two-dimensional Radiative Magnetohydrodynamic Simulations of Partial Ionization in the Chromosphere. II. Dynamics and Energetics of the Low Solar Atmosphere, *The Astrophysical Jour nal* **847** (2017) 36, https://doi.org/10.3847/1538-4357/aa8866

21. J. Martínez-Sykora *et al.*, On the generation of solar spicules and Alfvénic waves, *Science* **356** (2017) 1269, https://doi.org/10.1126/science.aah5412

22. B. D. Pontieu *et al.*, Observations and Numerical Models of Solar Coronal Heating Associated with Spicules, *The Astrophysical Journal Letters* **845** (2017) L18, https://dx.doi.org/10.3847/2041-8213/aa7fb4

23. K. Murawski, A. K. Srivastava, and T. V. Zaqarashvili, Numerical simulations of solar macrospicules, *Astronomy and Astrophysics* **535** (2011) A58, https://doi.org/10.1051/0004-6361/201117589

24. P. Kayshap *et al.*, Origin Ofmacrospicule And Jet In Polar Corona By A Small-Scale Kinked Flux Tube, *The Astrophysical Journal Letters* **770** (2013) L3, https://dx.doi.org/10.1088/2041-8205/770/1/L3

25. S. Kamio *et al.*, Observations of a rotating macrospicule associated with an X-ray jet, *Astronomy and Astrophysics* **510** (2010), https://doi.org/10.1051/0004-6361/200913269

26. N. E. Raouafi *et al.*, Solar Coronal Jets: Observations, Theory, and Modeling, *Space Science Reviews* **201** (2016), https://dx.doi.org/10.1007/s11214-016-0260-5

27. Y. Duan *et al.*, Macrospicules and Their Connection to Magnetic Reconnection in the Lower Solar Atmosphere, *The Astrophysical Journal Letters* **942** (2023), https://dx.doi.org/10.3847/2041-8213/

28. A. C. Sterling, Solar Spicules: A Review of Recent Models and Targets for Future Observations - (Invited Re view), *Sol Phys* **196** (2000) 79, https://doi.org/10.1023/A:1005213923962

29. W. Ruan, C. Xia, and R. Keppens, A Fully Self consistent Model for Solar Flares, *The Astrophysical Journal* **896** (2020) 97, https://doi.org/10.3847/1538-4357/ab93db

30. J. L. Giuliani, Jr., On the dynamics in evaporating cloud envelopes, *The Astrophysical Journal* **277** (1984) 605, https://doi.org/10.1086/161731

31. C. Levermore, Relating Eddington factors to flux limiters, *Journal of Quantitative Spectroscopy and Radiative Transfer* **31** (1984) 149, https://doi.org/10.1016/0022-4073(84)90112-2

32. R.-L. Jiang, C. Fang, and P.-F. Chen, Numerical Simulation of Solar Microflares in a Canopy-Type Magnetic Configuration, *The Astrophysical Journal* **751** (2012) 152, https://doi.org/10.1088/0004-637X/751/2/152

33. E. H. Avrett and R. Loeser, Models of the Solar Chromosphere and Transition Region from SUMER and HRTS Observations: Formation of the Extreme-Ultraviolet Spectrum of Hydrogen, Carbon, and Oxygen, *The Astrophysical Journal Supplement Series* **175** (2008) 229, https://dx.doi.org/10.1086/523671

34. J. D. M. Fuksman *et al.*, A Two-moment Radiation Hydrodynamics Scheme Applicable to Simulations of Planet Formation in Circumstellar Disks, *The Astro physical Journal* **906** (2021) 78, https://dx.doi.org/10.3847/1538-4357/abc879

35. D. Mihalas, Stellar Atmospheres, 2nd ed. (W. H. Freeman and Company, San Francisco, 1978), p. 632.

36. D. F. Gray, The Observation and Analysis of Stellar Photospheres, 3rd ed. (Cambridge University Press, Cambridge, UK, 2008), pp. 127-144.

37. G. B. Rybicki and A. P. Lightman, Radiative Processes in Astrophysics, 1st ed. (John Wiley and Sons, New York, NY, 1979), p. 400.

38. A. N. Cox, ed., Allen's Astrophysical Quantities, 4th ed. (Springer Science and BusinessMedia, New York, NY, 2000), pp. xviii + 719.

39. J. Leenaarts, Radiation hydrodynamics in simula tions of the solar atmosphere, *Living Reviews in Solar Physics* **17** (2020) 3, https://doi.org/10.1007/s41116-020-0024-x

40. V. Sukhorukov, A and J. Leenaarts, Partial redistribution in 3D non-LTE radiative transfer in solar atmosphere models, *Astronomy and Astrophysics* **597** (2017) A46, https://doi.org/10.1051/0004-6361/201629086

41. B. V. Gudiksen *et al.*, The stellar atmosphere simulation code Bifrost - Code description and validation, *Astronomy and Astrophysics* **531** (2011) A154, `https://doi.org/10.1051/0004-6361/201116520`

42. M. Carlsson and J. Leenaarts, Approximations for radiative cooling and heating in the solar chromosphere, *Astronomy and Astrophysics* **539** (2012) A39, `https://doi.org/10.1051/0004-6361/201118366`

43. N. Y. Gnedin and T. Abel, Multi-dimensional cosmological radiative transfer with a Variable Eddington Tensor formalism, *New Astronomy* **6** (2001) 437, `https://doi.org/10.1016/S1384-1076(01)00068-9`

44. M. González, E. Audit, and P. Huynh, HERACLES: a three-dimensional radiation hydrodynamics code, *Astronomy and Astrophysics* **464** (2007) 429, `https://doi.org/10.1051/0004-6361:20065486`

45. D. Aubert and R. Teyssier, A radiative transfer scheme for cosmological reionization based on a local Eddington tensor, *Monthly Notices of the Royal Astronomical Society* **387** (2008) 295, `https://doi.org/10.1111/j.1365-2966.2008.13223.x`

46. M. Petkova and V. Springel, A novel approach for accurate radiative transfer in cosmological hydrodynamic simulations, *Monthly Notices of the Royal Astronomical Society* **415** (2011) 3731, `https://doi.org/10.1111/j.1365-2966.2011.18986.x`

47. K. Murawski and T. V. Zaqarashvili, Numerical simulations of spicule formation in the solar atmosphere, *Astronomy and Astrophysic* **519** (2010) A8, `https://doi.org/10.1051/0004-6361/201014128`

48. A.Mignone *et al.*, PLUTO: A Numerical Code for Computational Astrophysics, *The Astrophysical Journal Supplement Series* **170** (2007) 228, `https://dx.doi.org/10.1086/513316`

49. T. Miyoshi and K. Kusano, A multi-state HLL approximate Riemann solver for ideal magnetohydro dynamics, *Journal of Computational Physics* **208** (2005) 315, `https://doi.org/10.1016/j.jcp.2005.02.017`

50. S. Li, An HLLC Riemann solver for magneto hydrodynamics, *Journal of Computational Physics* **203** (2005) 344, `https://doi.org/10.1016/j.jcp.2004.08.020`

51. D. S. Balsara and D. S. Spicer, A Staggered Mesh Algorithm Using High Order Godunov Fluxes to Ensure Solenoidal Magnetic Fields in Magnetohydrodynamic Simulations, *Journal of Computational Physics* **149** (1999) 270, `https://doi.org/10.1006/jcph.1998.6153`

52. J. D.M. Fuksman and A.Mignone, A Radiative Transfer Module for Relativistic Magnetohydrodynamics in the PLUTO Code, *The Astrophysical Journal Supplement Series* **242** (2019) 20, `https://dx.doi.org/10.3847/1538-4365/ab18ff`

53. U. M. Ascher, S. J. Ruuth, and R. J. Spiteri, Implicit1064 explicit Runge-Kutta methods for time-dependent partial differential equations, *Applied Numerical Mathematics* **25** (1997) 151, `https://doi.org/10.1016/S0168-9274(97)00056-1`

54. L. Pareschi and G. Russo, Implicit-Explicit Runge-Kutta Schemes and Applications to Hyperbolic Systems with Relaxation, *Journal of Scientific Computing* **25** (2005) 26, `https://doi.org/10.1007/s10915-004-4636-4`

55. V. Alexiades, G. Amiez, and P.-A. Gremaud, Super-timestepping acceleration of explicit schemes for parabolic problems, *Communications in Numerical Methods in Engineering* **12** (1996) 31, `https://doi.org/10.1002/(SICI)1099-0887(199601)12:1⟨31::AID-CNM950⟩3.0.CO;2-5`

56. K. Tanaka, Evolution of Chromospheric Fine Structures on the Disk, In R. G. Athay, ed., Chromospheric Fine Structure, vol. **56** of IAU Symposium (1974) p. 239, `https://ui.adsabs.harvard.edu/abs/1974IAUS...56..239T.`

57. I. S. Veselovsky, O. A. Panassenko, and S. Koutchmy, Solar plume formation in the solar corona, In T.- D. Guyenne, ed., Solar Jets and Coronal Plumes, vol. **421** of ESA Special Publication (1998) p. 345, `https://ui.adsabs.harvard.edu/abs/1998ESASP.421..345V.`

58. V. H. Hansteen *et al.*, Dynamic Fibrils Are Driven by Magnetoacoustic Shocks, *The Astrophysical Journal* **647** (2006) L73, `https://doi.org/10.1086/507452`

59. K. Wilhelm, Solar spicules and macrospicules observed by SUMER, *Astronomy and Astrophysic* **360** (2000) 351, `https://ui.adsabs.harvard.edu/abs/2000AandA...360..351W`

60. S. R. Habbal and R. D. Gonzalez, First Observations of Macrospicules at 4.8 GHz at the Solar Limb in Polar Coronal Holes, *The Astrophysical Journal Letters* **376** (1991) L25, `https://doi.org/10.1086/186094`

61. K. P. Dere *et al.*, CHIANTI - an atomic database for emission lines, Astron. Astrophys. *Suppl. Ser* **125** (1997) 149

62. C. R. Harris *et al.*, Array programming with NumPy, Nature **585** (2020), `https://doi.org/10.1038/s41586-020-2649-2`

63. J. D. Hunter, Matplotlib: A 2D graphics environment, *Computing in Science and Engineering* **9** (2007) 55, `https://doi.org/10.1109/MCSE.2007.55`

64. E. Ley-Koo, Recent progress in confined atoms and molecules: Superintegrability and symmetry breakings, *Rev. Mex. Fís.* **64** (2018) 326, `https://doi.org/10.31349/RevMexFis.64.326`

65. D. J. Griffiths, Introduction to electrodynamics, 2nd ed. (Prentice Hall, Englewood Cliffs, NJ, 1989), pp. 331-334.

66. B. De Pontieu, et al., A Tale of Two Spicules: The Impact of Spicules on the Magnetic Chromosphere*, *Publications of the Astronomical Society of Japan* **59** (2007) S655, `https://doi.org/10.1093/pasj/59.sp3.S655`

67. T. M. D. Pereira, B. De Pontieu, and M. Carlsson, Quantifying Spicules, *The Astrophysical Journal* **759** (2012) 18, `https://doi.org/10.1088/0004-637X/759/1/18`

68. H. Isobe *et al.*, Three-Dimensional Simulation of Solar Emerging Flux Using the Earth Simulator I. Magnetic Rayleigh-Taylor Instability at the Top of the Emerging Flux as the Origin of Filamentary Structure, *Publications of the Astronomical Society of Japan* **58** (2006) 423, `https://doi.org/10.1093/pasj/58.2.423`

69. S. Takasao, H. Isobe, and K. Shibata, Numerical Simulations of Solar Chromospheric Jets Associated with Emerging Flux, *Publications of the Astronomical Society of Japan* **65** (2013) 62, `https://doi.org/10.1093/pasj/65.3.62`

70. E. Pariat, S. K. Antiochos, and C. R. DeVore, A Model for Solar Polar Jets, *The Astrophysical Journal* **691** (2009) 61, `https://doi.org/10.1088/0004-637X/691/1/61`

71. V. Archontis, K. Tsinganos, and C. Gontikakis, Recurrent solar jets in active regions, *Astronomy and Astrophysics* **512** (2010) L2, `https://doi.org/10.1051/0004-6361/200913752`

72. F. Fang, Y. Fan, and S. W. McIntosh, Rotating Solar Jets in Simulations of Flux Emergence with Thermal Conduction, *The Astrophysical Journal Letters* **789** (2014) L19, `https://doi.org/10.1088/2041-8205/789/1/L19`

73. J. D. Melon Fuksman and A. Mignone, A Radiative Transfer Module for Relativistic Magnetohydrodynamics in the PLUTO Code, *The Astrophysical Journal Supplement Series* **242** (2019) 20, `https://doi.org/10.3847/1538-4365/ab18ff`

74. J. D. Melon Fuksman *et al.*, A Two-moment Radiation Hydrodynamics Scheme Applicable to Simulations of Planet Formation in Circumstellar Disks, *The Astrophysical Journal* **906** (2021) 78, `https://doi.org/10.3847/1538-4357/abc879`

75. E. Landi *et al.*, CHIANTI-An Atomic Database for Emission Lines. XII. Version 7 of the Database, *The Astrophysical Journal* **744** (2011) 99, `https://doi.org/10.1088/0004-637X/744/2/99`

76. K. P. Dere, The plasma filling factor of coronal bright points - II. Combined EIS and TRACE results, *Astronomy and Astrophysics* **497** (2009) 287, `https://doi.org/10.1051/0004-6361/200811329`

77. F. J. Rivera-Paleo and F. S. Guzmán, CAFE-R: A Code That Solves the Special Relativistic Radiation Hydrodynamics Equations, *The Astrophysical Journal Supplement Series* **241** (2019) 28, `https://doi.org/10.3847/1538-4365/ab0d8c`

78. H. Childs *et al.*, VisIt: An End-User Tool For Visualizing and Analyzing Very Large Data, In High Performance Visualization-Enabling Extreme-Scale Scientific Insight, pp. 357-372 (2012), `https://doi.org/10.1201/b12985`

79. J. D. Tanner, S. Basu, and P. Demarque, Comparing the Effect of Radiative Transfer Schemes on Convection Simulations, *The Astrophysical Journal* **759** (2012) 120, `https://doi.org/10.1088/0004-637X/759/2/120`

80. B. Commerçon *et al.*, Radiation hydrodynamics with adaptive mesh refinement and application to prestellar core collapse - I. Methods, *Astronomy and Astrophysics* **529** (2011) A35, `https://doi.org/10.1051/0004-6361/201015880`

81. C. Roedig, O. Zanotti, and D. Alic, General relativistic radiation hydrodynamics of accretion flows - II. Treating stiff source terms and exploring physical limitations, *Monthly Notices of the Royal Astronomical Society* **426** (2012) 1613, `https://doi.org/10.1111/j.1365-2966.2012.21821.x`

82. A. Sądowski *et al.*, Semi-implicit scheme for treating radiation under M1 closure in general relativistic conservative fluid dynamics codes, *Monthly Notices of the Royal Astronomical Society* **429** (2013) 3533, `https://doi.org/10.1093/mnras/sts632`

83. M. A. Skinner and E. C. Ostriker, A Two-moment Radiation Hydrodynamics Module in Athena Using a Time-explicit Godunov Method, *The Astrophysical Journal Supplement Series* **206** (2013) 21, `https://doi.org/10.1088/0067-0049/206/2/21`

84. H. R. Takahashi and K. Ohsuga, A Numerical Treatment of Anisotropic Radiation Fields Coupled with Relativistic Resistive Magnetofluids, *The Astrophysical Journal* **772** (2013) 127, `https://doi.org/10.1088/0004-637X/772/2/127`

85. J. C. McKinney *et al.*, Three-dimensional general relativistic radiation magnetohydrodynamical simulation of super-Eddington accretion, using a new code harmrad with M1 closure, *Monthly Notices of the Royal Astronomical Society* **441** (2014) 3177, `https://doi.org/10.1093/mnras/stu762`

86. P. V. Foukal, Solar Astrophysics, 1st ed. (Wiley Interscience, New York, 1990), p. 496.

87. J. T. Mariska and J. V. Hollweg, Alfvenic pulses in the solar atmosphere, *The Astrophysical Journal* **296** (1985) 746, `https://doi.org/10.1086/163491`

88. N. Guerreiro, M. Carlsson, and V. Hansteen, Numerical Simulations of Spicule Acceleration, *The Astrophysical Journal* **766** (2013) 128, `https://doi.org/10.1088/0004-637X/766/2/128`